nature materials

Article

https://doi.org/10.1038/s41563-025-02412-6

Real-space observation of flat-band ultrastrong coupling between optical phonons and surface plasmon polaritons

Received: 25 October 2024

Accepted: 17 October 2025

Published online: 18 December 2025

Check for updates

Edoardo Vicentini[1], Xabier Arrieta[2,3], Martin Schnell[1,4,5], Nicolas Pajusco[1,6], Felix Begemann[1], Maria Barra Burillo[1], Maria Ramos[1,2], Andrei Bylinkin[1], Ruben Esteban[2,4], Javier Aizpurua[3,4,5] & Rainer Hillenbrand[1,3,5]

Strong and ultrastrong coupling are pivotal phenomena in science and technology, where light–matter hybridization opens new avenues for manipulating quantum states, material properties or chemical reactions. Here we use pump–probe nanospectroscopy for real-space mapping of vibrational ultrastrong coupling between optical phonons in a thin SiC layer and surface plasmon polaritons in a semiconductor (InAs) substrate. By adjusting the InAs carrier density through photoexcitation, we align the flat dispersion limit of the surface plasmon polaritons to the SiC transverse optical phonon, yielding hybridized modes in an intriguingly wide wavevector range. This flat-band ultrastrong coupling contrasts conventional ultrastrong coupling, where hybridization typically occurs in a narrow wavevector range. We further predict flat-band coupling for weak oscillators, illustrated by strong coupling of molecular vibrations with low-loss surface phonon polaritons at their dispersion limit. Achieving strong and ultrastrong coupling over a large wavevector range, and thus many hybrid modes, may benefit polariton chemistry and phase transitions induced by strong and ultrastrong coupling.

The physical and chemical properties of atoms and molecules are governed by their energy levels. Tuning these levels can modify material properties and drive advancements in materials science, chemistry and photonics. A recent approach aims to leverage strong coupling (SC) and ultrastrong coupling (USC) between light and matter, where the mutual energy exchange (Rabi oscillations) creates hybrid light–matter states called polaritons[1–8]. Various optical matter excitations—including excitons, plasmons, phonons and molecular vibrations—can participate, benefiting applications ranging from ultrasensitive sensing to nonlinear optics and quantum technologies[9–14]. Of particular interest for controlling matter properties is vibrational strong coupling (VSC), where light couples to molecular or lattice vibrations (phonons). VSC has been reported to modify chemical reactivity[4,15,16] leading to polaritonic chemistry[5,6] and predicted to trigger phase transitions[17].

Either SC or USC (denoted (U)SC) can be achieved by coupling matter excitations with dispersive photonic modes, yielding anti-crossing and hybridization over a narrow wavevector range, that is, a limited number of hybrid states[1–8]. Here we employ nanoscale

[1]CIC nanoGUNE, Basque Research and Techology Alliance, Donostia–San Sebastián, Spain. [2]Centro de Física de Materiales (CFM-MPC), Consejo Superior de Investigaciones Científicas (CSIC) and Universidad del Pais Vasco – Euskal Herriko Unibertsitatea (UPV/EHU), Donostia–San Sebastián, Spain. [3]Department of Electricity and Electronics, University of the Basque Country, Leioa, Spain. [4]Donostia International Physics Center (DIPC), Donostia–San Sebastián, Spain. [5]Ikerbasque, the Basque Foundation for Science, Bilbao, Spain. [6]Laboratoire d'Acoustique de l'Université du Mans (LAUM), Institut d'Acoustique–Graduate School (IA-GS), CNRS and Le Mans Université, Le Mans, France. e-mail: r.hillenbrand@nanogune.eu

https://doi.org/10.1038/s41563-025-02412-6

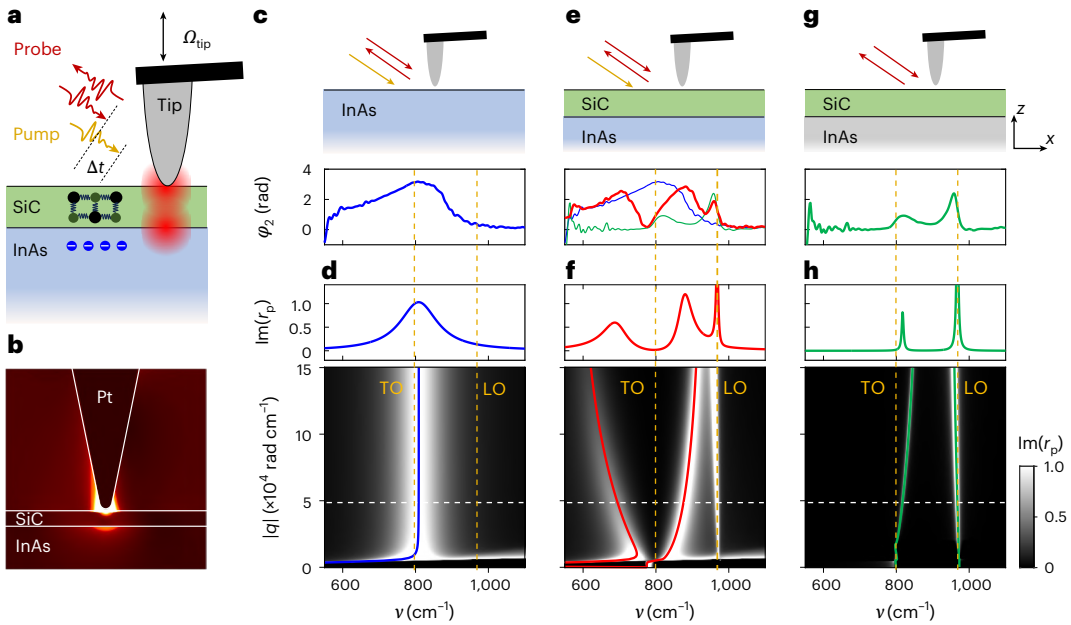

Fig. 1 | Pump–probe nano-FTIR spectroscopy of nanoscale USC between optical phonons and SPPs. a, Illustration of the experiment. Optical phonons in a 50-nm-thick SiC layer coupled with SPPs in a semi-infinite InAs substrate are excited by the near field of a mid-IR illuminated (incoming red arrow) metal tip oscillating at a frequency Ω_{tip}. This near-field coupling (red shaded area) is observed by recording the elastically tip-scattered light (outgoing red arrow) with an asymmetric Fourier transform spectrometer, yielding amplitude and phase-resolved spectra. For tuning the SPP resonance in InAs to match the TO phonon of SiC, a near-IR pump pulse (yellow arrow) is focused onto the sample to photoexcite carriers in the InAs substrate at a time Δt before the probe pulse. The near-IR pulse has 100 fs duration and a central wavelength of 1,550 nm. **b**, Numerical simulation showing the near-field distribution around the tip apex at 900 cm^{-1} when the SPP and TO phonon are ultrastrongly coupled. **c**,**e**,**g**, Measured nano-FTIR phase spectra $\varphi_2(\nu)$ of bare InAs at $\Delta t = 8.5$ ps (blue; **c**), SiC/InAs at $\Delta t = 8.5$ ps (red; **e**) and SiC/InAs without near-IR pump (green; **g**). Phase spectra are referenced to the phase spectra of unpumped bare InAs. The blue and green lines in **e** are the same as in **c** and **g**, respectively. **d**,**f**,**h**, Imaginary part of the calculated Fresnel reflection coefficient of the samples illustrated in **c**, **e** and **g**, respectively. The top shows $\mathrm{Im}[r_p(q_t,\nu)]$ at $q_t = 5 \times 10^4$ rad cm^{-1} (marked by horizontal dashed white line in bottom panel). The bottom shows $\mathrm{Im}[r_p(q,\nu)]$ as a function of real wavevector q and real frequency ν. Vertical dashed orange lines mark the TO and LO phonon frequencies of SiC. Blue, red and green curves in the bottom graph of **d**, **f** and **h** show the real part of the dispersion of modes, $\nu(q)$, assuming a complex-valued frequency. Optical material properties are in the Methods. In **d** and **f**, the plasma frequency and damping of carriers in InAs is $\nu_p = 845$ cm^{-1} and $\gamma_p = 115$ cm^{-1}, respectively, obtained by fitting the near-field spectrum in **c** (Supplementary Note 1). In **h**, $\varepsilon_{InAs}(\nu) = \varepsilon_{\infty,InAs}$.

Fourier transform infrared (nano-FTIR) spectroscopy to demonstrate that the number of (ultra)strongly coupled states can be increased by coupling optical excitations with surface polaritons that exhibit a flat dispersion—a scenario we term flat-band (U)SC. These findings lay the groundwork for future studies on how a larger amount of coupled states may enhance VSC-related phenomena.

VSC is typically achieved in matter-filled microcavities, but their large mode volumes hinder VSC with minute amounts of matter, crucial for accessing quantum regimes and for comparing with first-principles calculations of small systems. This can be overcome using ultraconfined propagating or localized plasmon or phonon polaritons in thin layers or nanostructures, whose small mode volumes enable VSC at the nanometre scale[18–24]. However, the wavevector mismatch between ultraconfined polaritons and free-space light challenges the far-field spectroscopy of individual nanoresonators. This problem can be circumvented by scattering-type scanning near-field optical microscopy (s-SNOM) and nano-FTIR spectroscopy, where the strong optical field concentration at the apex of a laser-illuminated metallic tip not only enables nanoscale spectroscopy and control of the VSC of single nanoresonators[25–27] but also spectroscopic polariton interferometry[23,28,29].

Here we report the nano-FTIR spectroscopy of optically tuned surface plasmon polaritons (SPPs) coupled to transverse optical (TO) phonons, demonstrating flat-band USC. We observe hybrid surface polaritons over an unusually large wavevector range, contrasting conventional (U)SC, where hybridization spans only a narrow range. Specifically, using pump–probe nano-FTIR[30], we study vibrational USC between infrared SPPs in a semi-infinite InAs substrate and TO phonons in a thin SiC layer atop InAs. A near-infrared (near-IR) pump tunes the InAs carrier concentration, aligning the SPP frequency with the SiC TO phonon. Nano-FTIR spectroscopy of the tip-excited SPP resonance[30–33] coupled to the SiC TO phonon shows nanoscale USC with a polariton splitting of about 20% at zero detuning, while momentum-resolved spectral nanoimaging reveals hybrid polaritons across a remarkably large momentum range. Dispersion calculations and coupled harmonic oscillator analysis let us explain this finding by the coupling of two excitations with flat dispersion—the SiC TO phonon and the InAs SPP at its dispersion limit. Finally, we theoretically predict flat-band SC with molecular vibrations, which may open new opportunities for polariton chemistry.

Results

Figure 1a illustrates the pump–probe nano-FTIR spectroscopy of a 50-nm-thick SiC layer on an undoped InAs substrate (hereafter SiC/InAs sample). An ~100 fs, 1,550 nm, 25 mW pump beam (orange arrow) is focused onto an atomic force microscopy (AFM) tip, which photoexcites electrons in the undoped InAs and thus creates a transient carrier density that decays on a picosecond timescale. As a result, the carrier concentration, n, temporarily reaches ~10^{18}–10^{19} cm^{-3} (and affects the plasma frequency $\nu_p \propto \sqrt{n}$), sufficient to support mid-infrared SPPs in InAs (refs. 30,34). To probe the SPPs and their coupling with the SiC phonons, broadband 100 fs mid-IR laser pulses are focussed onto the tip at a controllable time delay Δt relative to the pump pulse. The Δt value determines a specific plasma frequency ν_p and damping rate γ_p

and is selected to align the InAs SPP with the SiC TO phonon. Due to the lightning rod effect, the AFM tip with apex radius (R) ≈ 30 nm concentrates the mid-IR probe (red arrow) to a nanoscale near-field spot at its apex, as illustrated by the numerical simulation shown in Fig. 1b. This near field enables the excitation of surface polaritons at momenta far beyond the reach of the far-field spectroscopy of unstructured samples[35]. For probing the SPPs and their coupling with the SiC phonons, the elastically scattered mid-IR radiation from the tip (red arrow) is recorded by Fourier transform spectroscopy. Since the surface polariton lifetime (on the order of picoseconds) is shorter than the timescale over which ν_p and γ_p vary (Supplementary Fig. 1c), both parameters can be considered as constant during the phonon lifetime. To suppress the background, the tip is oscillated at a frequency of Ω_{tip}, and the mid-IR detector signal is demodulated at $2\Omega_{tip}$. Interferograms are obtained by recording the demodulated detector signal as a function of the reference mirror position in the spectrometer. Fourier transforming these interferograms yields background-free amplitude and phase spectra, $s_2(\nu)$ and $\varphi_2(\nu)$, where ν is the frequency in wavenumbers and the subscript 2 denotes the demodulation order. In Fig. 1 we analyse phase spectra, as they resemble extinction spectra and can be interpreted accordingly.

We first characterize the InAs SPPs to establish a SPP resonance around the SiC TO phonon (797 cm^{-1}). To that end, we record nano-FTIR spectra of the bare InAs substrate for various probe–pump delays Δt (Supplementary Fig. 1). For Δt = 8.5 ps, $\varphi_2(\nu)$ shows a peak around 810 cm^{-1} (blue curve in Fig. 1c), aligning with the SiC TO phonon. This peak corresponds to a SPP resonance excited by the near fields at the tip apex[30,33,35]. To study the coupling between the SPP resonance and the phonons in SiC, we perform pump–probe nano-FTIR spectroscopy of the SiC/InAs sample at Δt = 8.5 ps (Fig. 1e). We observe a remarkably large splitting (red spectrum) of the SPP resonance (blue spectrum) of about 180 cm^{-1}, which, being >20% of the TO phonon frequency ν_{TO}, indicates USC. For comparison, we show $\varphi_2(\nu)$ of the SiC/InAs sample without photoexcitation (Fig. 1e,g, green curves). We observe one peak slightly above the TO phonon and another near the longitudinal optical (LO) phonon of SiC, which we attribute to the surface phonon polariton (SPhP) resonances of the thin SiC layer in the absence of InAs SPPs, similar to observations in $SrTiO_3$ layers[36]. We note that the peak near LO also appears in the red spectrum shown in Fig. 1e, but its coupling with the InAs SPP is negligible. Further, the peaks are non-Lorentzian, which is typical for nano-FTIR spectroscopy[35] and not a disorder effect that can challenge coupling-strength extraction[37]. In fact, the optical phonon of our single-crystal SiC is well described by a single Lorentz oscillator[38].

To validate the experimental results, we compare the nano-FTIR phase spectra $\varphi_2(\nu)$ with the calculated (Methods) imaginary part of the samples' reflection coefficient[23,36,39–41], Im[$r_p(q_t,\nu)$], where q_t is the dominant in-plane wavevector of the tip's near field that probes r_p (top of Fig. 1d,f,h). For the standard tips used in our experiments, $q_t \approx 5\times10^4$ rad cm^{-1} (ref. 42). While the comparison between nano-FTIR and reflection spectra is qualitative, it avoids the modelling of polariton-resonant near-field interactions in layered samples, which often lacks quantitative accuracy[36]. In the top of Fig. 1d, we show Im[$r_p(q_t,\nu)$] of the photoexcited bare InAs substrate, confirming that it describes well the SPP peak in $\varphi_2(\nu)$ (Fig. 1c). We subsequently calculate Im[$r_p(q_t,\nu)$] of the photoexcited SiC/InAs sample (top of Fig. 1f), corroborating the peak splitting observed in $\varphi_2(\nu)$ (Fig. 1e). Analogue calculations in Fig. 1h confirm the SPhP peaks when InAs is not photoexcited. The calculations also confirm that the peak near LO is minimally affected by the SPP, and therefore it will not be considered further.

Aiming for a more comprehensiveunderstanding of the near-field spectra, we show in Fig. 1d,f,h the calculated (Methods) wavevector (q)-dependent and frequency-dependent reflection coefficients, Im[$r_p(q,\nu)$] (greyscale map) and surface polariton dispersions (solid lines on greyscale map). For the photoexcited bare InAs (Fig. 1d), we observe the SPP mode at its dispersion limit (ν_{SPP} = 780 cm^{-1}), and for the unpumped SiC/InAs, we observe the upper and lower SPhP modes of the SiC layer[38] on undoped InAs (Fig. 1h, bottom). For the photoexcited SiC/InAs sample (Fig. 1f, bottom), we find two modes that are largely shifted below and above $\nu_{SPP} \approx \nu_{TO}$, indicating USC between the TO phonon and SPP. Intriguingly, the anti-crossing of these two hybrid surface polariton modes appears over an unusually wide wavevector range, rather than over a comparatively narrow range typical for USC.

To verify the unusual USC phenomenon, we probe the hybrid surface polariton dispersion through real-space polariton interferometry[28,34,43] (Fig. 2a). That is, we record nano-FTIR amplitude and phase spectra, $s_2(x,\nu)$ and $\varphi_2(x,\nu)$, while scanning the photoexcited sample perpendicular to the SiC edge (x direction). The SPP resonance is tuned to the SiC TO phonon frequency by adjusting the time delay to Δt = 15 ps. This delay differs slightly from Fig. 1e, likely due to a pump intensity variation caused by scattering of the pump beam at the SiC edge. As illustrated in Fig. 2a, the mid-IR near fields at the tip apex launch hybrid surface polaritons (red horizontal arrow; electric field E_p) on the photoexcited sample, which reflect at the SiC edge and interfere at the tip apex with the incoming electric field E_{inc}, leading to a variation of s_2 and φ_2. In the referenced and filtered amplitude-resolved and phase-resolved spectral line scan, $s_2^*(x,\nu)$ and $\varphi_2^*(x,\nu)$ (Fig. 2d and Supplementary Note 2), we observe intensity maxima and minima near the SiC edge (x = 0), which vanish far from the edge. To corroborate that these signal variations originate from damped polaritons propagating in the x direction, and to determine their wavevector, we analyse $s_2^*(x,\nu)$ and $\varphi_2^*(x,\nu)$ for each frequency (Fig. 2b and Supplementary Note 3). The corresponding complex-valued near-field profiles, $\sigma_2^*(x) = s_2^*(x)\,e^{i\varphi_2^*(x)}$, trace spiral paths around a complex-valued offset C (dots in Fig. 2c), which can be fitted by a model of radially propagating damped waves[44,45] (Methods and solid lines in Fig. 2b,c), confirming tip-launched surface polaritons. The short propagation lengths arise from the dissipation and low group velocities associated with the flat polariton dispersion[33,38,40,45]. Interestingly, the spirals are anticlockwise below TO and clockwise above, indicating negative and positive phase velocities, respectively[46].

Fitting $\sigma_2^*(x,\nu)$ yields the wavevector $\tilde{q}_\pm(\nu) = q_\pm(\nu) + i\kappa_\pm(\nu)$ of the hybrid surface polaritons (Methods and Supplementary Note 3), whose real part reveals the polariton dispersion (red and blue dots indicate positive and negative phase velocity, respectively). To compare with theory, we fit $\tilde{q}_\pm(\nu)$ to the calculated hybrid surface polariton dispersion, using the InAs plasma frequency ν_p and damping γ_p as fitting parameters (Supplementary Note 4). For ν_p = 850 cm^{-1} and γ_p = 120 cm^{-1}, the calculated (curves) and experimental (dots) dispersions in Fig. 2e match well, confirming upper and lower polariton branches. These branches cross neither the SiC TO phonon (horizontal dashed line) nor the SPhP dispersion of unpumped SiC/InAs (green dots in Fig. 2e,g) for $q > 10^4$ rad cm^{-1}. The SPhP dispersion of unpumped SiC/InAs is obtained from $s_2^*(x,\nu)$ and $\varphi_2^*(x,\nu)$ maps without the near-IR pump (Fig. 2f), showing polariton fringes only above TO. Analysis of complex-valued line profiles yields the SPhP dispersion (green dots in Fig. 2g,e), which is confirmed by dispersion calculations (green curve in Fig. 2g).

To gain deeper insight into the coupling mechanism, we analyse $\tilde{q}_\pm(\nu)$ (red and blue curves in Fig. 2e), obtained from the experimental measurements (dots in Fig. 2e), using a coupled classical harmonic oscillator model describing USC[22,47,48]. This model relates the hybrid modes with the two bare (uncoupled) modes, each represented by a harmonic oscillator. Since, within the model, all modes are described with a complex-valued frequency and a real-valued wavevector, $\tilde{q}_\pm(\nu)$ obtained from Fig. 2e is transformed into $\tilde{\nu}_\pm(q)$ (red curves in Fig. 3). One of the bare modes is attributed to the SPP, whose dispersion, $\tilde{\nu}_{SPP}(q)$, is calculated from the poles of the reflection coefficient of the SiC/InAs heterostructure using ν_p and γ_p obtained from the fit in Fig. 2e.

https://doi.org/10.1038/s41563-025-02412-6

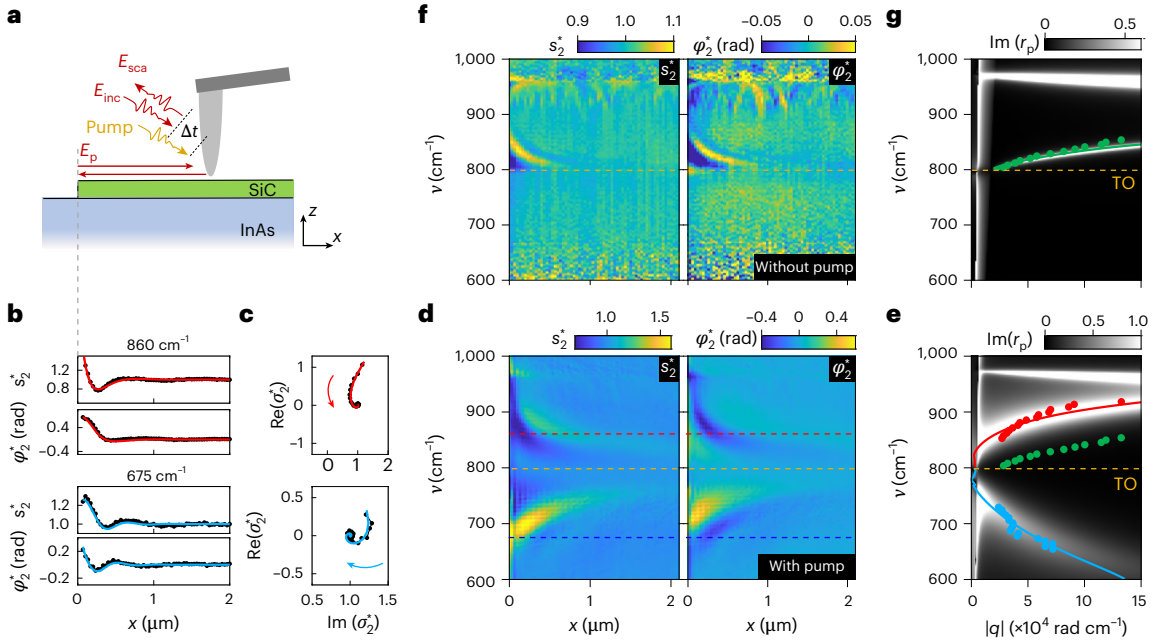

Fig. 2 | Real-space mapping of flat-band USC. a, Illustration of surface polariton mapping on a 50-nm-thick SiC layer on an InAs substrate. E_{inc} is the incoming field, E_{sca} the scattered field, and E_p the surface polariton field. **b**, Baseline-subtracted near-field amplitude and phase signal as function of x at $\nu = 675$ cm^{-1} and 860 cm^{-1}. **c**, Line profiles of **b** plotted in the complex plane. In **b** and **c**, black dots and solid lines represent experimental data and fits, respectively. **d**, Amplitude and phase spectra of the tip-scattered field, $s_2^*(x, \nu)$ and $\varphi_2^*(x, \nu)$, recorded as a function of distance from the edge, x, for pump–probe delay of $\Delta t = 15$ ps. Red and blue dashed lines mark the frequencies of the line profiles shown in **b** and **c**. In **b**–**d**, spatial filtering is applied for better visibility of the polariton fringes (Supplementary Note 2). **e**, Red and blue dots show the absolute value of the real part of the hybrid surface polariton wavevector, $q_\pm(\nu)$, obtained by complex-valued fitting the spatial line profiles in **b** at each ν value. Red and blue colours indicate positive and negative signs of q, respectively. Green dots are the same as in **g**. Greyscale contour plot shows the calculated Im[$r_p(q,\nu)$], using $\nu_p = 850$ cm^{-1} for InAs. **f**, Amplitude and phase spectra of the tip-scattered field $s_2^*(x, \nu)$ and $\varphi_2^*(x, \nu)$, recorded as a function of x without the pump beam. **g**, Green dots show the real part of the surface polariton wavevector, $q_{SPhP}(\nu)$, obtained by complex-valued fitting the spatial line profiles in **f** at each ν value. Greyscale contour plot shows the calculated Im[$r_p(q,\nu)$] (same as in Fig. 1h). In **d**–**g**, orange dashed lines mark the TO phonon frequency of SiC. In **e** and **g**, red, blue and green curves show the absolute value of the real part of the mode dispersions, $q_\pm$ and q_{SPhP}, assuming a complex-valued wavevector, corresponding to the poles of $r_p(q + i\kappa, \nu)$ (Methods and Supplementary Note 4).

To account for dielectric loading caused by the high-frequency permittivity of the SiC layer, $\varepsilon_{\infty,SiC}$, we set $\varepsilon_{SiC} = \varepsilon_{\infty,SiC}$. The remaining bare mode, ν_E, is determined from

$$\nu_\pm = \frac{1}{\sqrt{2}}\sqrt{\nu_{SPP}^2 + \nu_E^2 + 4g^2 \pm \sqrt{\left(\nu_{SPP}^2 + \nu_E^2 + 4g^2\right)^2 - 4\nu_{SPP}^2\nu_E^2}}, \quad (1)$$

which relates bare and hybrid modes through the coupling strength g. We note that equation (1) does not consider losses, as they are negligible for determining coupling strength and mode frequencies, as verified by repeating the analysis with losses included (Supplementary Note 8). Solving equation (1) for ν_E and g at each q, we obtain $\nu_E(q) \approx \nu_{TO}(q)$ (black curve in Fig. 3a), showing that the hybrid modes can be understood as the result of coupling between the InAs SPP and the SiC TO phonon[22]. Further, we find that (1) g increases with q, (2) the SC condition according to $g > (\gamma_{SPP} + \gamma_{TO})/4$ is fulfilled for all $q > 1 \times 10^4$ rad cm^{-1} and (3) USC occurs for all $q > 1 \times 10^4$ rad cm^{-1} according to $g > 0.1\nu_{TO}$ (Fig. 3c). γ_{SPP} and γ_{TO} are the damping rates of the SPP and the TO phonon, respectively. We also calculate the relative contribution of the SPP, Σ_{SPP}, and that of the TO phonon of SiC, Σ_{TO}, to the hybrid surface polaritons, finding that the SPP contributes to the lower polariton (marked ν_- in Fig. 3a) with Σ_{SPP} between 50% and 30% in the whole wavevector region with $q > 1 \times 10^4$ rad cm^{-1} (Fig. 3b and Supplementary Note 7). Our analysis thus corroborates the vibrational USC between SPPs and TO phonons.

Importantly, the analysis confirms hybrid polariton modes over an unusually large wavevector range. This stems from the relatively flat SPP dispersion near the SiC TO phonon at large q (blue curve in Fig. 3a). We thus refer to the observed phenomenon as flat-band vibrational USC. Although perfect matching with the TO phonon occurs only at one wavevector, q_c, the detuning of the SPP mode from the TO phonon is relatively small compared with the splitting Ω of the hybrid modes. Thus, coupling with nearly 30 to 70% contribution from the SPP and the TO phonon is maintained over a large wavevector range.

The slight redshift of the SPP mode with increasing wavevector q arises from its growing confinement to the InAs surface, and thus inside SiC, corresponding to an increased dielectric loading of the SPP. Figure 3a shows this via the normalized vertical electric field intensity profile, $|E(q,z)|^2$ (Methods), of the bare SPP mode.

The increasing spatial overlap between the bare SPP field and the SiC layer also accounts for the rise in coupling strength g with increasing q. We quantify this effect by calculating g from the ratio of the electric field energy of the bare SPP mode within the SiC layer to its total electromagnetic energy[47,48] (equation (15) and Methods). The result (dotted line in Fig. 3c) excellently matches g obtained from the coupled harmonic oscillator model and corroborates its increase with q (solid line in Fig. 3c). We note that the drop of g below the light line is irrelevant, as the surface polariton modes are not defined there.

To verify the flat-band USC phenomenon in a simplified system that avoids SPP detuning at large q, we repeat the theoretical analysis of Fig. 3a–c for a SiC half-space instead of a 50-nm-thin layer (Fig. 3d–f). Because the SPP field above the InAs is, for all wavevectors, fully confined within the SiC, the SPP mode (blue curve in Fig. 3d) exhibits a nearly horizontal dispersion at large wavevectors. Consequently, the hybrid modes (red curves in Fig. 3d) exhibit a horizontal dispersion.

https://doi.org/10.1038/s41563-025-02412-6

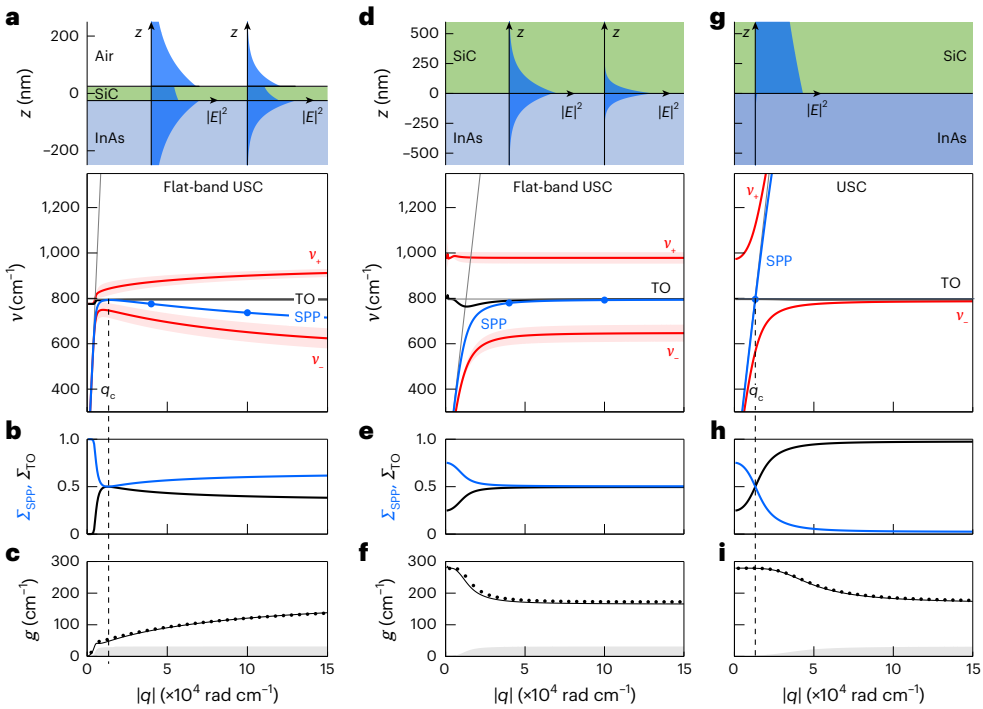

Fig. 3 | Theoretical analysis of flat-band USC between SPPs and TO phonons. **a**, Illustration of a 50-nm-thick SiC layer on an InAs substrate with $\nu_p = 850$ cm^{-1}, $\gamma_p = 120$ cm^{-1} and $\varepsilon_{\infty,InAs} = 11.8$. Blue areas show calculated electric field profiles $|E(q,z)|^2$ of the bare SPP modes at 4×10^4 and 10×10^4 rad cm^{-1} when the SiC layer is substituted by a layer of the same thickness and permittivity $\varepsilon_{\infty,SiC}$. **d**, Illustration of fully SiC-filled upper half-space above InAs substrate with $\nu_p = 995$ cm^{-1}, $\gamma_p = 120$ cm^{-1} and $\varepsilon_{\infty,InAs} = 11.8$. Blue areas show calculated electric field profiles $|E(q,z)|^2$ of the bare SPP modes at $q = 4 \times 10^4$ and 10×10^4 rad cm^{-1} for upper half-space permittivity $\varepsilon_{\infty,SiC}$. **g**, Illustration of fully SiC-filled upper half-space above InAs substrate with $\nu_p = 3{,}000$ cm^{-1}, $\gamma_p = 120$ cm^{-1} and $\varepsilon_{\infty,InAs} = 11.8$. Blue areas show calculated electric field profiles of the bare SPP mode at $q = 1.3 \times 10^4$ rad cm^{-1} for an upper half-space permittivity $\varepsilon_{\infty,SiC}$. In **a**, **d** and **g**, the red curves show the dispersion of upper and lower hybrid modes, $\nu_+(q)$ and $\nu_-(q)$. Reddish areas indicate damping of the hybrid modes, $\nu_+(q) \pm \gamma_+(q)/2$ and $\nu_-(q) \pm \gamma_-(q)/2$. Blue curves show bare SPP dispersion when the SiC is substituted by a material with permittivity $\varepsilon_{\infty,SiC}$. Black lines show ν_E, matching the TO phonon frequency (grey horizontal line) of SiC. Grey solid lines show the light line. **b**,**e**,**h**, Contribution of SPPs (blue curves) and of TO phonons (black curves) to the hybrid modes $\nu_-(q)$ shown in **a**, **d** and **g**, respectively. **c**,**f**,**i**, Coupling strength, $g(q)$, obtained from **a**, **d** and **g**, respectively. Solid lines show results obtained from coupled harmonic oscillator model. Dotted lines show results obtained from equation (15). Grey and white areas indicate weak and strong coupling regimes, respectively. The strong coupling regime is determined by $g > (\gamma_{SPP} + \gamma_{TO})/4$, where $\gamma_{TO} = 6$ cm^{-1} and γ_{SPP} is determined experimentally as described in Supplementary Note 6. Vertical dashed black lines mark wavevector where bare modes cross, q_c.

Analysis using the coupled harmonic oscillator model reveals that the SPP and TO phonon each contribute equally (~50%) to the hybrid modes for all wavevectors larger than ~3×10^4 rad cm^{-1} (Fig. 3e). Further, $g = 170$ cm^{-1} remains constant (solid line in Fig. 3f), as confirmed by calculating g via equation (15) (dotted line in Fig. 3f).

To better appreciate the unique features of the flat-band USC, Fig. 3g–i compares the conventional anti-crossing of hybrid modes (red) when the uncoupled bare modes (blue and black) cross at an individual wavevector q_c. To that end, the InAs plasma frequency is shifted to $\nu_p = 3{,}000$ cm^{-1}. We observe that the SPP and TO phonon are ultrastrongly coupled, but the ν_+ and ν_- modes anti-cross over only a narrow wavevector range around q_c, reverting to uncoupled modes for $q > q_c$. Coupled harmonic oscillator analysis reveals nearly equal SPP and TO phonon contributions to the hybrid modes only within the narrow anti-crossing region (Fig. 3h). By contrast, for flat-band vibrational USC (Fig. 3d,e), the hybrid modes remain strongly shifted from the uncoupled modes even for large q, with both the SPP and TO phonon contributing substantially to the hybrid modes.

We finally predict flat-band VSC with organic molecules by coupling low-loss substrate surface polaritons to molecular vibrations in a thin organic layer with dielectric function $\varepsilon_{M1}(\tilde{\nu})$ (Fig. 4a). We consider SPhPs on SiC (25 times lower damping than InAs SPPs) and set the molecular resonance M1 to $\nu_{M1} = 921.3$ cm^{-1} near the SiC surface-phonon frequency $\nu_{SPh} = 921.9$ cm^{-1}. To assume realistic values for the oscillator strength, damping and high-frequency permittivity $\varepsilon_{\infty,M1}$ (Methods), we use those values corresponding to pentacene molecules[49]. To prevent a redshift of the SPhP with increasing q, we set the permittivity of the upper half-space to $\varepsilon_{\infty,M1}$. The hybrid modes, $\nu_\pm(q)$ (red solid lines, Fig. 4a), are nearly horizontal and parallel to the SPhP dispersion for $q > 3 \times 10^4$ rad cm^{-1}, with ~50/50 contributions (Fig. 4b) and g fulfilling the SC criterion (Fig. 4c). By comparison, Fig. 4d–f shows conventional anti-crossing after shifting the molecular vibration M2 to $\nu_{M2} = 880$ cm^{-1}. The hybrid modes anti-cross only near q_c and turn to the uncoupled modes at larger q (Fig. 4e). In this scenario, nearly equal contributions from SPhPs and molecular vibrations occur only within the narrow anti-crossing region, unlike in flat-band VSC, where both contribute strongly across a large wavevector range.

Discussion

The flat dispersion of the hybrid modes arises because the substrate surface polaritons coupling with TO phonons or molecular vibrations approach their dispersion limit, making them increasingly matter-like. Consequently, our findings might be interpreted as (ultra-)strong matter–matter coupling, rather than conventional light–matter coupling in microcavities or systems with substantial photon contribution. Further, flat-band SC and USC feature small group velocities, limiting polariton transport. However, the enhanced number of coupled polariton states may benefit applications aimed at modifying material properties via VSC. Note that aligning the SPP dispersion limit with the TO phonon may also be achieved through substrate doping.

https://doi.org/10.1038/s41563-025-02412-6

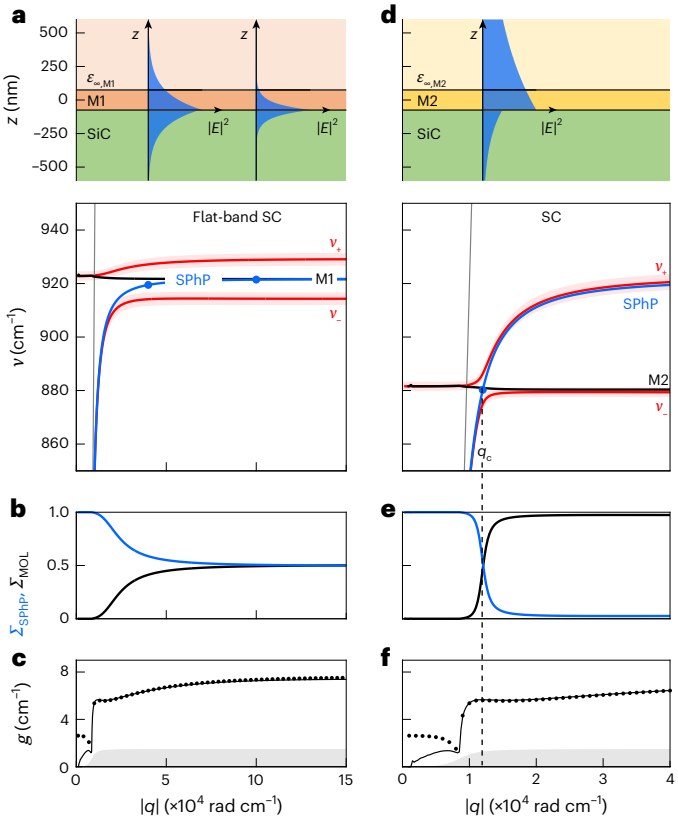

Fig. 4 | Theoretical analysis of flat-band SC between SPhPs and molecular vibrations. a,**d**, Sketches in upper row illustrate the heterostructures analysed in the corresponding columns. **a**, A 150-nm-thick layer of molecules with $\nu_{M1} = 921.3\ cm^{-1}$, $\gamma_{M1} = 3.5\ cm^{-1}$ and $\varepsilon_{\infty,M1} = 2.98$ on SiC substrate. The permittivity of the upper half-space is $\varepsilon_{\infty,M1}$. Blue areas show calculated electric field profiles $|E(q,z)|^2$ of the bare SPhP modes at $q = 4 \times 10^4$ and $10 \times 10^4\ rad\ cm^{-1}$ when the molecular layer is substituted by a layer of the same thickness and permittivity $\varepsilon_{\infty,M1}$. **d**, A 150-nm-thick layer of molecules with $\nu_{M2} = 880\ cm^{-1}$, $\gamma_{M2} = 3.5\ cm^{-1}$ and $\varepsilon_{\infty,M2} = 2.98$ on a SiC substrate. The permittivity of the upper half-space is $\varepsilon_{\infty,M2}$. Blue areas show calculated electric field profiles of the bare SPhP modes at $q = 1.2 \times 10^4\ rad\ cm^{-1}$ for a layer permittivity $\varepsilon_{\infty,M2}$. In **a** and **d**, red curves show dispersion of upper and lower hybrid modes, $\nu_+(q)$ and $\nu_-(q)$. Reddish areas indicate damping of the hybrid modes, $\nu_+(q) \pm \gamma_+(q)/2$ and $\nu_-(q) \pm \gamma_-(q)/2$. Blue curves show the dispersion of SPhPs on SiC substrate in the presence of a 150-nm-thick layer with permittivity $\varepsilon_{\infty,M2}$. Black lines show ν_E, matching the molecular vibrational frequencies ν_{Mi}. Grey lines indicate the light line inside the upper half-space with $q = k_0/\sqrt{\varepsilon_{\infty,Mi}}$, where k_0 is the free-space wavevector of light. **b**,**e**, Contribution of SPhPs (blue curve) and of molecular vibrations (black curves) to the hybrid mode $\nu_-(q)$ shown in **a** and **d**, respectively. **c**,**f**, Coupling strength, $g(q)$, obtained from **a** and **d**, respectively. Solid lines show the results obtained from the harmonic oscillator model. Dotted lines show the results obtained from equation (15). Grey and white areas indicate weak and strong coupling regimes, respectively. The strong coupling regime is determined by $g > (\gamma_{SPhP} + \gamma_{Mi})/4$ where $\gamma_{M1} = \gamma_{M2} = 3.5\ cm^{-1}$ and γ_{SPhP} is determined according to ref. 38. In **d**, **e** and **f**, the vertical dashed black lines indicate the wavevector where bare modes cross, q_c.

Our results resemble plasmon–phonon coupling in polar semiconductors, where plasmons and optical phonons coexist within the same material and coupling can be tuned via doping[50] or photoexcitation[51]. In such materials, flat-band USC may be achieved too, potentially modifying electron–phonon scattering[52]. By contrast, our approach is more versatile, as surface plasmons and phonons reside in separate materials and couple across their interface. This enables flat-band USC of phonons in materials that do not support plasmon polaritons or where variation of carrier concentration cannot tune the SPP dispersion limit to the phonon frequency.

In summary, we use pump–probe nano-FTIR spectroscopy to study the coupling between TO phonons in a thin SiC layer and SPPs in a bulk InAs substrate. By tuning the SPP dispersion limit through photoexcitation of carriers in InAs to align with the TO phonon, we observe hybrid polaritons emerging from USC (mode splitting > 20%). Remarkably, the hybrid modes span an extraordinarily broad momentum range, introducing the concept of flat-band USC. We predict that flat-band VSC could also be achieved with molecular vibrations.

Flat-band vibrational SC and USC could be relevant to emerging research exploring strong coupling to modify chemical and physical material properties[4–6,15,16]. Unlike conventional SC, which involves few hybrid states, flat-band SC and USC feature many hybrid polaritons, potentially amplifying polariton chemistry. In the context of ultrafast SPhP control via femtosecond laser excitation of the substrate[34], our study shows that USC can largely enhance the modulation of polariton wavevectors. In our experiments, hybrid surface polariton wavevectors change by over an order of magnitude (Supplementary Note 9), far exceeding the 20% reported in the literature[34], opening new opportunities for ultrafast polaritonic sensing and circuitry.

Online content

Any methods, additional references, Nature Portfolio reporting summaries, source data, extended data, supplementary information, acknowledgements, peer review information; details of author contributions and competing interests; and statements of data and code availability are available at https://doi.org/10.1038/s41563-025-02412-6.

References

1. Galego, J., Garcia-Vidal, F. J. & Feist, J. Cavity-induced modifications of molecular structure in the strong-coupling regime. *Phys. Rev. X* **5**, 041022 (2015).
2. Garcia-Vidal, F. J., Ciuti, C. & Ebbesen, T. W. Manipulating matter by strong coupling to vacuum fields. *Science* **373**, eabd0336 (2021).
3. Forn-Díaz, P., Lamata, L., Rico, E., Kono, J. & Solano, E. Ultrastrong coupling regimes of light-matter interaction. *Rev. Mod. Phys.* **91**, 025005 (2019).
4. Hutchison, J. A., Schwartz, T., Genet, C., Devaux, E. & Ebbesen, T. W. Modifying chemical landscapes by coupling to vacuum fields. *Angew. Chem. Int. Ed.* **51**, 1592–1596 (2012).
5. Nagarajan, K., Thomas, A. & Ebbesen, T. W. Chemistry under vibrational strong coupling. *J. Am. Chem. Soc.* **143**, 16877–16889 (2021).
6. Xiang, B. & Xiong, W. Molecular polaritons for chemistry, photonics and quantum technologies. *Chem. Rev.* **124**, 2512–2552 (2024).
7. Frisk Kockum, A., Miranowicz, A., De Liberato, S., Savasta, S. & Nori, F. Ultrastrong coupling between light and matter. *Nat. Rev. Phys.* **1**, 19–40 (2019).
8. Baranov, D. G. et al. Ultrastrong coupling between nanoparticle plasmons and cavity photons at ambient conditions. *Nat. Commun.* **11**, 2715 (2020).
9. Stassi, R. et al. Quantum nonlinear optics without photons. *Phys. Rev. A* **96**, 023818 (2017).
10. Sentef, M. A., Ruggenthaler, M. & Rubio, A. Cavity quantum-electrodynamical polaritonically enhanced electron-phonon coupling and its influence on superconductivity. *Sci. Adv.* **4**, eaau6969 (2018).
11. Stassi, R. & Nori, F. Long-lasting quantum memories: extending the coherence time of superconducting artificial atoms in the ultrastrong-coupling regime. *Phys. Rev. A* **97**, 033823 (2018).
12. Chikkaraddy, R. et al. Single-molecule strong coupling at room temperature in plasmonic nanocavities. *Nature* **535**, 127–130 (2016).
13. Tame, M. S. et al. Quantum plasmonics. *Nat. Phys.* **9**, 329–340 (2013).

14. Ruggenthaler, M., Tancogne-Dejean, N., Flick, J., Appel, H. & Rubio, A. From a quantum-electrodynamical light–matter description to novel spectroscopies. *Nat. Rev. Chem.* **2**, 0118 (2018).
15. Vergauwe, R. M. A. et al. Modification of enzyme activity by vibrational strong coupling of water. *Angew. Chem. Int. Ed.* **58**, 15324–15328 (2019).
16. Thomas, A. et al. Tilting a ground-state reactivity landscape by vibrational strong coupling. *Science* **363**, 615–619 (2019).
17. Ashida, Y. et al. Quantum electrodynamic control of matter: cavity-enhanced ferroelectric phase transition. *Phys. Rev. X* **10**, 041027 (2020).
18. Autore, M. et al. Boron nitride nanoresonators for phonon-enhanced molecular vibrational spectroscopy at the strong coupling limit. *Light Sci. Appl.* **7**, 17172 (2018).
19. Menghrajani, K. S., Nash, G. R. & Barnes, W. L. Vibrational strong coupling with surface plasmons and the presence of surface plasmon stop bands. *ACS Photon.* **6**, 2110–2116 (2019).
20. Dayal, G., Morichika, I. & Ashihara, S. Vibrational strong coupling in subwavelength nanogap patch antenna at the single resonator level. *J. Phys. Chem. Lett.* **12**, 3171–3175 (2021).
21. Autore, M. et al. Enhanced light–matter interaction in ^{10}B monoisotopic boron nitride infrared nanoresonators. *Adv. Optical Mater.* **9**, 2001958 (2021).
22. Yoo, D. et al. Ultrastrong plasmon–phonon coupling via epsilon-near-zero nanocavities. *Nat. Photon.* **15**, 125–130 (2021).
23. Bylinkin, A. et al. Real-space observation of vibrational strong coupling between propagating phonon polaritons and organic molecules. *Nat. Photon.* **15**, 197–202 (2021).
24. Liu, K. et al. Vibrational strong coupling between surface phonon polaritons and organic molecules via single quartz micropillars. *Adv. Mater.* **34**, 2109088 (2022).
25. Dolado, I. et al. Remote near-field spectroscopy of vibrational strong coupling between organic molecules and phononic nanoresonators. *Nat. Commun.* **13**, 6850 (2022).
26. Muller, E. A. et al. Nanoimaging and control of molecular vibrations through electromagnetically induced scattering reaching the strong coupling regime. *ACS Photon.* **5**, 3594–3600 (2018).
27. Hirschmann, O., Bhakta, H. H., Kort-Kamp, W. J. M., Jones, A. C. & Xiong, W. Spatially resolved near field spectroscopy of vibrational polaritons at the small N limit. *ACS Photon.* **11**, 2650–2658 (2024).
28. Ni, G. X. et al. Ultrafast optical switching of infrared plasmon polaritons in high-mobility graphene. *Nat. Photon.* **10**, 244–247 (2016).
29. Wehmeier, L. et al. Landau-phonon polaritons in Dirac heterostructures. *Sci. Adv.* **10**, eadp3487 (2024).
30. Wagner, M. et al. Ultrafast dynamics of surface plasmons in InAs by time-resolved infrared nanospectroscopy. *Nano Lett.* **14**, 4529–4534 (2014).
31. Knoll, B. & Keilmann, F. Infrared conductivity mapping for nanoelectronics. *Appl. Phys. Lett.* **77**, 3980–3982 (2000).
32. Hillenbrand, R., Taubner, T. & Keilmann, F. Phonon-enhanced light–matter interaction at the nanometre scale. *Nature* **418**, 159–162 (2002).
33. Stiegler, J. M. et al. Nanoscale free-carrier profiling of individual semiconductor nanowires by infrared near-field nanoscopy. *Nano Lett.* **10**, 1387–1392 (2010).
34. He, M. et al. Polariton design and modulation via van der Waals/doped semiconductor heterostructures. *Nat. Commun.* **14**, 7965 (2023).
35. Hillenbrand, R., Abate, Y., Liu, M., Chen, X. & Basov, D. N. Visible-to-THz near-field nanoscopy. *Nat. Rev. Mater.* **10**, 285–310 (2025).
36. Xu, R. et al. Highly confined epsilon-near-zero and surface phonon polaritons in $SrTiO_3$ membranes. *Nat. Commun.* **15**, 4743 (2024).
37. Schwennicke, K., Giebink, N. C. & Yuen-Zhou, J. Extracting accurate light–matter couplings from disordered polaritons. *Nanophotonics* **13**, 2469–2478 (2024).
38. Mancini, A. et al. Near-field retrieval of the surface phonon polariton dispersion in free-standing silicon carbide thin films. *ACS Photon.* **9**, 3696–3704 (2022).
39. Fei, Z. et al. Infrared nanoscopy of Dirac plasmons at the graphene–SiO_2 interface. *Nano Lett.* **11**, 4701–4705 (2011).
40. Dai, S. et al. Tunable phonon polaritons in atomically thin van der Waals crystals of boron nitride. *Science* **343**, 1125–1129 (2014).
41. Passler, N. C. et al. Strong coupling of epsilon-near-zero phonon polaritons in polar dielectric heterostructures. *Nano Lett.* **18**, 4285–4292 (2018).
42. Hauer, B., Engelhardt, A. P. & Taubner, T. Quasi-analytical model for scattering infrared near-field microscopy on layered systems. *Opt. Express* **20**, 13173–13188 (2012).
43. Huber, M. A. et al. Femtosecond photo-switching of interface polaritons in black phosphorus heterostructures. *Nat. Nanotechnol.* **12**, 207–211 (2017).
44. Chen, S. et al. Real-space nanoimaging of THz polaritons in the topological insulator Bi_2Se_3. *Nat. Commun.* **13**, 1374 (2022).
45. Chen, S. et al. Real-space observation of ultraconfined in-plane anisotropic acoustic terahertz plasmon polaritons. *Nat. Mater.* **22**, 860–866 (2023).
46. Yoxall, E. et al. Direct observation of ultraslow hyperbolic polariton propagation with negative phase velocity. *Nat. Photon.* **9**, 674–678 (2015).
47. Barra-Burillo, M. et al. Microcavity phonon polaritons from the weak to the ultrastrong phonon–photon coupling regime. *Nat. Commun.* **12**, 6206 (2021).
48. Muniain, U., Aizpurua, J., Hillenbrand, R., Martín-Moreno, L. & Esteban, R. Description of ultrastrong light–matter interaction through coupled harmonic oscillator models and their connection with cavity-QED Hamiltonians. *Nanophotonics* **14**, 2031–2052 (2025).
49. Schubert, M., Bundesmann, C., Jacopic, G., Maresch, H. & Arwin, H. Infrared dielectric function and vibrational modes of pentacene thin films. *Appl. Phys. Lett.* **84**, 200–202 (2004).
50. Bryxin, V. V., Mirlin, D. N. & Reshina, I. I. Surface plasmon-phonon interaction in n-InSb. *Solid State Commun.* **11**, 695–699 (1972).
51. Dunkelberger, A. D. et al. Active tuning of surface phonon polariton resonances via carrier photoinjection. *Nat. Photon.* **12**, 50–56 (2018).
52. Hagenmüller, D., Schachenmayer, J., Genet, C., Ebbesen, T. W. & Pupillo, G. Enhancement of the electron–phonon scattering induced by intrinsic surface plasmon–phonon polaritons. *ACS Photon.* **6**, 1073–1081 (2019).

Methods

Sample preparation

A commercially available 50-nm-thick 3C-phase SiC membrane (Norcada) is controllably fractured from its frame using a viscoelastic polydimethyl-siloxane (PDMS) stamp, by placing the stamp over the whole membrane and steadily pulling it away. The resulting pieces typically have lateral sizes of tens of micrometres. They remain on the PDMS stamp surface, from which they are transferred onto an undoped InAs substrate (dry-transfer method).

Pump–probe nano-FTIR spectroscopy

We use a commercial s-SNOM set-up equipped with a pump–probe module (neaSNOM, Attocube Systems), in which the oscillating (at a frequency $\Omega_{tip} \approx 270$ kHz with 75 nm tapping amplitude) metal-coated (Pt/Ir) AFM tip (nano-FTIR tips from Attocube Systems) is illuminated by focused p-polarized near-IR pump pulses (central wavelength 1.55 µm, ~100 fs pulse duration, average power of about 25 mW) and p-polarized broadband mid-IR probe pulses (supercontinuum laser with ~100 fs pulse duration, average power of about 0.5 mW, frequency range 600–1,200 cm^{-1}). The time delay Δt between the probe and pump pulses is adjusted via an optical delay line. Both beams are focused onto the tip apex with a parabolic mirror. The tip-scattered mid-IR probe radiation is collected with the same parabolic mirror and recorded with an asymmetric Fourier transform spectrometer comprising a liquid-nitrogen-cooled mercury–cadmium–telluride (MCT) detector. To suppress background scattering from the tip shaft and the sample, the detector signal is demodulated at frequency $n\Omega_{tip}$. Recording of the demodulated detector signal as a function of the reference mirror position yields interferograms, which are Fourier transformed to obtain amplitude $s_n(\nu)$ and phase $\varphi_n(\nu)$ spectra. To filter the near-IR pump laser, a long-wavelength pass filter is placed in front of the MCT detector. The signal-to-noise ratio of the commercial set-up is improved via a balanced detection scheme[53].

The interferograms (signal demodulation at $2\Omega_{tip}$) yielding the phase spectra in Fig. 1c,e,g are recorded with 1,024 sampling points, 20 ms integration time and a spectral resolution of 7.14 cm^{-1}. The spectra are obtained by Fourier transform of the zero-padded interferograms extended to 4,028 points, without applying an apodization window.

The interferograms (signal demodulation at $2\Omega_{tip}$) yielding the spectra in Fig. 2d,f are recorded with 1,024 sampling points, 5 ms integration time and a spectral resolution of 6.25 cm^{-1}. The complex-valued spectra, $\sigma_2(x,\nu)$, are obtained by Fourier transform of the zero-padded interferograms extended to 4,028 points, without applying an apodization window. The line scans are acquired with a spatial step size (pixel size) of 33 nm, covering a total scan length of 5 µm with 150 pixels. Each line scan is repeated 12 times and averaged after realignment of the tip position relative to the SiC edge, which is determined from the simultaneously recorded topography signal. The complex-valued near-field spectra are referenced to the complex-valued near-field spectrum of the SiC/InAs sample far away from the SiC edge and filtered according to the procedure described in Supplementary Note 2, yielding $\sigma_2^*(x,\nu)$.

Complex-valued fitting of nano-FTIR line profiles

To determine the complex-valued hybrid surface polariton wavevector, $\tilde{q}_\pm(\nu) = q_\pm(\nu) + i\kappa_\pm(\nu)$, we construct complex-valued line profiles, $\sigma_2^*(x,\nu) = s_2^*(x,\nu)\,e^{i\varphi_2^*(x,\nu)}$, from the filtered (Supplementary Note 2) referenced amplitude-resolved and phase-resolved spectral line scans, $s_2^*(x,\nu)$ and $\varphi_2^*(x,\nu)$, and fit them for each frequency using the following equation:

$$E(x) = \frac{A}{\sqrt{2x}} e^{i2(q_\pm + i\kappa_\pm)x} + \frac{B}{\sqrt{2x}} e^{i2(q_{bl} + i\kappa_{bl})x} + 1. \quad (2)$$

Equation (2) describes the field of two radially propagating damped waves launched at the tip apex, which are reflected at the edge of the SiC layer[44,45,54]. The first term describes the hybrid surface polariton with wavevector $q_\pm + i\kappa_\pm$. The second term, characterized by a wavevector $q_{bl} + i\kappa_{bl}$, is referred to as baseline (bl). It is constrained to $q_{bl} < 2k_0$, where k_0 is the photon wavevector in free space. The inclusion of the second term is justified by the spatial Fourier transform of the line scan (Supplementary Note 2), which reveals spectral intensity near the light line. The third term (offset of 1) accounts for the near-field signal far away from the SiC edge.

A and B are complex-valued fit parameters, whereas $q_\pm$, $\kappa_\pm$, q_{bl} and κ_{bl} are real-valued fit parameters. To mitigate potential parameter interdependence, we apply a sequential fitting strategy (Supplementary Note 3).

In Fig. 2b,c of the main text, we show baseline-corrected experimental data, $\sigma_2^*(x) - B/\sqrt{2x}e^{i2(q_{bl}+i\kappa_{bl})x}$ (black dots), together with the fit, $A/\sqrt{2x}e^{i2(q_\pm+i\kappa_\pm)x} + 1$ (solid lines). The $|q(\nu)|$ is shown by the dots in Fig. 2e,g. The fitting procedure is demonstrated in Supplementary Note 3.

Calculation of reflection coefficients

The reflection coefficient (p polarization) for layered samples (Figs. 1f,h and 2e,g) is calculated according to

$$r_p(q,\nu) = \frac{r_{p,12}(q,\nu) + r_{p,23}(q,\nu)\,e^{2ik_{z,2}(q,\nu)d}}{1 + r_{p,12}(q,\nu)\,r_{p,23}(q,\nu)\,e^{2ik_{z,2}(q,\nu)d}} \quad (3)$$

where $r_{p,ab}(q,\nu)$ is the Fresnel reflection coefficient between layers j and l given by

$$r_{p,jl}(q,\nu) = \frac{\varepsilon_l(\nu)\,k_{z,j}(q,\nu) - \varepsilon_j(\nu)\,k_{z,l}(q,\nu)}{\varepsilon_l(\nu)\,k_{z,j}(q,\nu) + \varepsilon_j(\nu)\,k_{z,l}(q,\nu)} \quad (4)$$

with q being the in-plane wavevector, ν the frequency expressed as wavenumber, $k_{z,j}$ the out-of-plane wavevector $k_{z,j}(q,\nu) = \sqrt{\varepsilon_j(\nu)k_0^2(\nu) - q^2}$, $\varepsilon_j(\nu)$ the complex-valued permittivity of the material j, d the thickness of layer 2, and k_0 the photon wavevector in free space. The indices 1, 2 and 3 indicate upper half-space, layer and substrate, respectively, as illustrated in Supplementary Fig. 5a.

The reflection coefficient (p polarization) for the bare InAs substrate (Fig. 1d) is calculated with equation (4). The indices j and l in this case stand for air and InAs, respectively; $\varepsilon_j = 1$ and $\varepsilon_l = \varepsilon_{InAs}(\nu)$.

A summary of all the parameters used in the reflection coefficient calculation of Figs. 1–4 is provided in Supplementary Tables 1 and 2.

Dispersion calculations

To calculate the dispersion of the surface polariton modes (solid lines in Figs. 1f,h, 2e,g, 3a and 4a,d) in a layer on a semi-infinite substrate (illustrated in Supplementary Fig. 5a), we find numerically the poles of the reflection coefficient by setting the denominator of equation (3) to zero:

$$1 + r_{p,12}(\tilde{q},\tilde{\nu})\,r_{p,23}(\tilde{q},\tilde{\nu})\,e^{2ik_{z,2}(\tilde{q},\tilde{\nu})d} = 0. \quad (5)$$

To calculate the dispersion of the surface polariton modes (blue solid lines in Figs. 1d, 3d,g and 4a,d and red solid lines in Fig. 3d,g) on the semi-infinite substrates (illustrated in Supplementary Fig. 5b), we find numerically the poles of the reflection coefficient by setting the denominator of equation (4) to zero:

$$\frac{k_{z,2}(\tilde{q},\tilde{\nu})}{\varepsilon_2(\tilde{\nu})} + \frac{k_{z,3}(\tilde{q},\tilde{\nu})}{\varepsilon_3(\tilde{\nu})} = 0. \quad (6)$$

We note that both equations (5) and (6) are expressed in a general form with complex-valued wavevectors defined as $\tilde{q} = q + i\kappa$ and complex-valued frequencies defined as $\tilde{\nu} = \nu - i\gamma/2$, but they are numerically solved by assuming either real-valued wavevectors or real-valued frequencies.

The dispersion curves shown in Figs. 1d,f,h, 3a,d,g and 4a,d are obtained by solving equations (5) and (6) numerically for temporally decaying modes, as we aim for a comparison with spectroscopy experiments that correspond to measurements of polaritons oscillating and decaying in time. To that end, we assume complex-valued frequencies and real-valued wavevectors, $\nu - i\gamma/2$ and q, respectively. The dispersion curves display the real part of the solution $q(\nu - i\gamma/2)$.

The dispersion curves shown in Fig. 2e,g are obtained by solving equations (5) and (6) numerically for spatially decaying modes, as we aim for a comparison with polariton interferometry experiments where we observe and analyse propagating and spatially decaying polaritons. For that end, we assume real-valued frequencies and complex-valued wavevectors, ν and $q + i\kappa$, respectively. The dispersion curves display the real part of the solution, $q(\nu)$.

To calculate the hybrid surface polariton modes, $\nu_{\pm}(q) - i\gamma_{\pm}(q)/2$, shown in Fig. 3a (red solid lines), we solve equation (5) for $\varepsilon_1 = 1$, $\varepsilon_2 = \varepsilon_{SiC}(\tilde{\nu})$ and $\varepsilon_3 = \varepsilon_{InAs}(\tilde{\nu})$. To calculate the bare SPP mode, $\nu_{SPP}(q) - i\gamma_{SPP}(q)/2$, shown in Fig. 3a (blue solid line), we solve equation (5) for $\varepsilon_1 = 1$, $\varepsilon_2 = \varepsilon_{\infty,SiC}$ and $\varepsilon_3 = \varepsilon_{InAs}(\tilde{\nu})$.

To calculate the hybrid surface polariton mode, $\nu_{\pm}(q) - i\gamma_{\pm}(q)/2$, shown in Fig. 3d,g (red solid lines), we solve equation (6) for $\varepsilon_2 = \varepsilon_{SiC}(\tilde{\nu})$ and $\varepsilon_3 = \varepsilon_{InAs}(\tilde{\nu})$. To calculate the bare SPP mode, $\nu_{SPP}(q) - i\gamma_{SPP}(q)/2$, shown in Fig. 3d,g (blue solid line), we solve equation (6) for $\varepsilon_2 = \varepsilon_{\infty,SiC}$ and $\varepsilon_3 = \varepsilon_{InAs}(\tilde{\nu})$.

To calculate the hybrid surface polariton mode, $\nu_{\pm}(q) - i\gamma_{\pm}(q)/2$, shown in Fig. 4a,d (red solid lines), we solve equation (5) for $\varepsilon_1 = \varepsilon_{\infty,Mi}$, $\varepsilon_2 = \varepsilon_{Mi}(\tilde{\nu})$ and $\varepsilon_3 = \varepsilon_{SiC}(\tilde{\nu})$. To calculate the bare SPhP mode, $\nu_{SPhP}(q) - i\gamma_{SPhP}(q)/2$, shown in Fig. 3d,g (blue solid line), we solve equation (6) for $\varepsilon_2 = \varepsilon_{\infty,Mi}$ and $\varepsilon_3 = \varepsilon_{SiC}(\tilde{\nu})$.

A summary of all the parameters used in the dispersion calculation of Figs. 1–4 is provided in Supplementary Tables 1 and 2.

Material parameters

The permittivity of the 3C-SiC layer is described by a Drude–Lorentz model:

$$\varepsilon_{SiC}(\tilde{\nu}) = \varepsilon_{\infty,SiC}\frac{\tilde{\nu}^2 - \nu_{LO}^2 + i\gamma_{TO}\tilde{\nu}}{\tilde{\nu}^2 - \nu_{TO}^2 + i\gamma_{TO}\tilde{\nu}} \quad (7)$$

where $\nu_{TO} = 797\ cm^{-1}$ and $\nu_{LO} = 973\ cm^{-1}$ are the TO and LO phonon frequencies, $\gamma_{TO} = 6\ cm^{-1}$ the damping constants and $\varepsilon_{\infty,SiC} = 6.6$ the high-frequency permittivity[38]. The thickness of the SiC layer is $d = 50$ nm.

The permittivity of the InAs is described by a Drude model:

$$\varepsilon_{InAs}(\tilde{\nu}) = \varepsilon_{\infty,InAs}\left(1 - \frac{\nu_p^2}{\tilde{\nu}^2 + i\tilde{\nu}\gamma_p}\right) \quad (8)$$

where ν_p is the plasma frequency, γ_p is the damping constant and $\varepsilon_{\infty,InAs} = 11.8$ the high-frequency permittivity[55].

For the undoped InAs in Figs. 1h and 2g, we set $\varepsilon_{InAs}(\tilde{\nu}) = \varepsilon_{\infty,InAs}$.

For the photoexcited InAs in Fig. 1d,f, we set $\nu_p = 845\ cm^{-1}$ and $\gamma_p = 125\ cm^{-1}$. Both plasma frequency and damping were determined from the experimental measurements described in Supplementary Note 1.

For the photoexcited InAs in Figs. 2e and 3a, we set $\nu_p = 850\ cm^{-1}$ and $\gamma_p = 120\ cm^{-1}$. Both plasma frequency and damping were determined from the experimental measurements described in Supplementary Note 4.

For the InAs in Fig. 3d, we set $\nu_p = 995\ cm^{-1}$ and $\gamma_p = 120\ cm^{-1}$, while for the InAs in Fig. 3g, we set $\nu_p = 3{,}000\ cm^{-1}$ and $\gamma_p = 120\ cm^{-1}$.

The permittivity values of the molecular layers, ε_{M1} in Fig. 4a and ε_{M2} in Fig. 4d, are described by

$$\varepsilon_{Mi}(\tilde{\nu}) = \varepsilon_{\infty,Mi}\left(1 - \frac{A_{Mi}^2/\varepsilon_{\infty,Mi}}{\tilde{\nu}^2 - \nu_{Mi}^2 + i\gamma_{Mi}\tilde{\nu}}\right) \quad (9)$$

where $\varepsilon_{\infty,M1} = \varepsilon_{\infty,M2} = 2.98$ is the high-frequency permittivity, $\nu_{M1} = 921.3\ cm^{-1}$ and $\nu_{M2} = 880\ cm^{-1}$ the molecular vibrational frequencies, $\gamma_{M1} = \gamma_{M2} = 3.5\ cm^{-1}$ the damping constants and $A_{M1} = A_{M2} = 91.5\ cm^{-1}$ the oscillator strengths. The thickness of the molecular layers is $d = 150$ nm. To assume realistic values for oscillator strength, damping and high-frequency permittivity, we use those corresponding to pentacene molecules ($C_{22}H_{14}$) at $905.5\ cm^{-1}$ (Table 1 in ref. 49).

A summary of all the material parameters is provided in Supplementary Table 2.

Relative contributions of SPP and TO phonon to hybrid surface polariton modes

The relative contributions of the SPP and TO phonon to the hybrid modes (shown in Fig. 3b,e,h), Σ_{SPP} and Σ_{TO}, respectively, are obtained according to[48]

$$\Sigma_{SPP}(\nu_{\pm}) = \frac{|x_{SPP}(\nu_{\pm})|^2}{|x_{SPP}(\nu_{\pm})|^2 + |x_{TO}(\nu_{\pm})|^2} = \frac{\left|\frac{x_{SPP}(\nu_{\pm})}{x_{TO}(\nu_{\pm})}\right|^2}{\left|\frac{x_{SPP}(\nu_{\pm})}{x_{TO}(\nu_{\pm})}\right|^2 + 1}$$

$$\Sigma_{TO}(\nu_{\pm}) = \frac{|x_{TO}(\nu_{\pm})|^2}{|x_{SPP}(\nu_{\pm})|^2 + |x_{TO}(\nu_{\pm})|^2} = \frac{1}{\left|\frac{x_{SPP}(\nu_{\pm})}{x_{TO}(\nu_{\pm})}\right|^2 + 1} \quad (10)$$

where x_{SPP} and x_{TO} are the oscillator amplitudes associated with the bare SPP and TO phonon modes, and

$$\frac{x_{SPP}}{x_{TO}} = -\frac{2gi\nu_{\pm}}{\left(\nu_{SPP}^2 - \nu_{\pm}^2\right)}. \quad (11)$$

In Supplementary Note 7, we compare the results of classical and quantum mechanical harmonic oscillator calculations.

Harmonic oscillator modelling of the coupling between molecular vibrations and SPhPs

To analyse how the hybrid surface polariton modes ν_+ and ν_- (red curves, solutions of equation (5) in Fig. 4a,d) emerge from the coupling between the SPhPs of the SiC substrate and the molecular vibrations of the organic layer, we applied the classical model of two coupled harmonic oscillators as described in the main text (Supplementary Note 7). One harmonic oscillator represents the SPhP with eigenmode frequency ν_{SPhP} and the other one represents the molecular vibration with eigenmode frequency ν_{Mi}. The relative contribution of SPhPs and molecular vibrations (shown in Fig. 4b,e) is calculated analogously to equation (10).

Calculation of the surface polariton field profiles

To calculate the spatial electric field distribution of the bare surface polaritons in Figs. 3a and 4a,d, we use the solution of Maxwell's equations for a transverse magnetic electromagnetic wave propagating along the surface (geometry defined by Supplementary Fig. 5a). The magnetic field, $\mathbf{H} = (0, H_y, 0)$, is expressed by

$$H_{y,1}(q,x,z) = A(q)e^{-k_{z,1}(q)\left[z-\frac{d}{2}\right]}e^{iqx},\ z > d/2$$

$$H_{y,2}(q,x,z) = B(q)e^{k_{z,2}(q)\left[z-\frac{d}{2}\right]}e^{iqx} + C(q)e^{-k_{z,2}(q)\left[z+\frac{d}{2}\right]}e^{iqx},\ -d/2 > z > d/2 \quad (12)$$

$$H_{y,3}(q,x,z) = D(q)e^{k_{z,3}(q)\left[z+\frac{d}{2}\right]}e^{iqx},\ z < -d/2,$$

where d is the thickness of the layer (index $j = 2$) on top of the substrate (index $j = 3$), $k_{z,j}$ is the out-of-plane wavevector $k_{z,j}(q) = \sqrt{q^2 - \varepsilon_j(\tilde{\nu})k_0^2(\tilde{\nu})}$,

$\varepsilon_j(\tilde{\nu}(q))$ is the complex-valued permittivity, $k_0(\tilde{\nu}(q))$ is the photon wavevector in free space and $\tilde{\nu}(q)$ is the complex-valued frequency of the calculated mode at q. Index $j = 1$ indicates the half-space above the layer. To remain consistent with the analysis of Figs. 3 and 4, we adopt complex-valued frequencies and real-valued wavevectors. Applying boundary conditions, the field amplitudes A, B, C and D can be mutually related. In particular, we write A, B and C as a function of D according to

$$A = D\frac{2\frac{k_{z,2}}{\varepsilon_2}e^{-k_{z,2}d}}{\frac{k_{z,1}}{\varepsilon_1}+\frac{k_{z,2}}{\varepsilon_2}+\left(-\frac{k_{z,1}}{\varepsilon_1}+\frac{k_{z,2}}{\varepsilon_2}\right)e^{-2k_{z,2}d}}$$

$$B = D\frac{\left(-\frac{k_{z,1}}{\varepsilon_1}+\frac{k_{z,2}}{\varepsilon_2}\right)e^{-k_{z,2}d}}{\frac{k_{z,1}}{\varepsilon_1}+\frac{k_{z,2}}{\varepsilon_2}+\left(-\frac{k_{z,1}}{\varepsilon_1}+\frac{k_{z,2}}{\varepsilon_2}\right)e^{-2k_{z,2}d}}$$

$$C = D\frac{\left(\frac{k_{z,1}}{\varepsilon_1}+\frac{k_{z,2}}{\varepsilon_2}\right)}{\frac{k_{z,1}}{\varepsilon_1}+\frac{k_{z,2}}{\varepsilon_2}+\left(-\frac{k_{z,1}}{\varepsilon_1}+\frac{k_{z,2}}{\varepsilon_2}\right)e^{-2k_{z,2}d}} \quad (13)$$

We subsequently obtain the electric field, $\mathbf{E} = (E_x, 0, E_z)$, according to $E_{x,j}(q,x,z) = \frac{-i}{\tilde{\nu}\varepsilon_0}\frac{1}{\varepsilon_j}\frac{dH_y}{dz}$ and $E_{z,j}(q,x,z) = \frac{i}{\tilde{\nu}\varepsilon_0}\frac{1}{\varepsilon_j}\frac{dH_y}{dx}$, where ε_0 is the vacuum permittivity.

The electric field profiles $|E_j(q,z)|^2 = |E_{x,j}(q,0,z)|^2 + |E_{z,j}(q,0,z)|^2$ of the bare SPPs in Fig. 3a are calculated using $\varepsilon_1(\tilde{\nu}) = 1$, $\varepsilon_2(\tilde{\nu}) = \varepsilon_{\infty,\mathrm{SiC}}$, $\varepsilon_3(\tilde{\nu}) = \varepsilon_{\mathrm{InAs}}(\tilde{\nu})$ and $d = 50$ nm. The complex-valued frequencies $\tilde{\nu}(q) = \nu_{\mathrm{SPP}}(q) - i\gamma_{\mathrm{SPP}}(q)/2$ are calculated according to equation (5).

Similarly, to calculate the surface polariton fields shown in Fig. 3d,g, we express the magnetic field as $\mathbf{H} = (0, H_y, 0)$, with

$$H_{y,2}(q,x,z) = Ae^{-k_{z,2}(q)z}e^{iqx},\ z > 0$$

$$H_{y,3}(q,x,z) = Be^{+k_{z,3}(q)z}e^{iqx},\ z < 0. \quad (14)$$

Applying boundary conditions, we find that the field amplitudes A and B must satisfy $A = B$.

The electric field profiles $|E_j(q,z)|^2 = |E_{x,j}(q,0,z)|^2 + |E_{z,j}(q,0,z)|^2$ of the bare SPPs shown in Fig. 3d,g are calculated using $\varepsilon_2(\tilde{\nu}) = \varepsilon_{\infty,\mathrm{SiC}}$ and $\varepsilon_3(\tilde{\nu}) = \varepsilon_{\mathrm{InAs}}(\tilde{\nu})$. The bare SPhP is calculated using $\varepsilon_2(\tilde{\nu}) = \varepsilon_{\infty,\mathrm{M1}}$ and $\varepsilon_3\left(\tilde{\nu}\right) = \varepsilon_{\mathrm{SiC}}\left(\tilde{\nu}\right)$ in Fig. 4a, and using $\varepsilon_2(\tilde{\nu}) = \varepsilon_{\infty,\mathrm{M2}}$ and $\varepsilon_3(\tilde{\nu}) = \varepsilon_{\mathrm{SiC}}(\tilde{\nu})$ in Fig. 4d. The complex-valued frequencies $\tilde{\nu}(q) = \nu_{\mathrm{SPP/SPhP}}(q) - i\gamma_{\mathrm{SPP/SPhP}}(q)/2$ are calculated according to equation (6).

To facilitate visualization and comparison, the surface polariton field intensities, $|E(q,z)|^2$, are normalized to the maximum value of 1 in each panel.

Calculation of coupling strength g based on energy ratios

We calculate the coupling strength between the bare SPPs of the InAs substrate and the TO phonons in SiC (black dots in Fig. 3c,f,i) according to[47,56]

$$g(q) = g_{\max}\sqrt{\frac{2W_{\mathrm{SPP,layer}}(q)}{U_{\mathrm{SPP}}(q)}}, \quad (15)$$

where $W_{\mathrm{SPP,layer}}$ is the SPP electric field energy per unit area in the SiC layer (Fig. 3c) or SiC half-space (Fig. 3f,i) when the SiC permittivity is replaced by $\varepsilon_{\infty,\mathrm{SiC}}$. It is given by

$$W_{\mathrm{SPP,layer}}(q) = \int_{\mathrm{SiC}}\frac{\varepsilon_0}{4}\varepsilon_{\infty,\mathrm{SiC}}\left(|E_x(q,z)|^2 + |E_z(q,z)|^2\right)dz. \quad (16)$$

U_{SPP} is the total electromagnetic energy per unit area of the SPP field given by

$$U_{\mathrm{SPP}}(q) = \int_{-\infty}^{+\infty}\left(\frac{\varepsilon_0}{4}\frac{d(\nu\mathrm{Re}[\varepsilon(\nu,z)])}{d\nu}\Big|_{\mathrm{Re}[\nu_{\mathrm{SPP}}(q)]}\left(|E_x(q,z)|^2 + |E_z(q,z)|^2\right) + \frac{\mu_0}{4}|H_y(q,z)|^2\right)dz, \quad (17)$$

where $\varepsilon(\nu,z)$ represents the dielectric function of each material, specifically $\varepsilon_1 = 1$, $\varepsilon_2 = \varepsilon_{\infty,\mathrm{SiC}}$ and $\varepsilon_3 = \varepsilon_{\mathrm{InAs}}(\nu)$ in Fig. 3c and $\varepsilon_2 = \varepsilon_{\infty,\mathrm{SiC}}$ and $\varepsilon_3 = \varepsilon_{\mathrm{InAs}}(\nu)$ in Fig. 3f,i. The maximum coupling strength, $g_{\max} = \sqrt{\left(\nu_{\mathrm{LO}}^2 - \nu_{\mathrm{TO}}^2\right)/4}$, corresponds to that of light–matter coupling in infinite-size bulk[47] SiC. The coupling strength between the bare SPhPs and molecular vibrations, shown in Fig. 4c,f, is calculated analogously, but with $g_{\max} = \sqrt{(A_{\mathrm{Mi}}^2/\varepsilon_{\infty,\mathrm{Mi}})/4}$.

Data availability

The data, plotting scripts and complementary description of the calculations used in this study are openly available via Zenodo at https://doi.org/10.5281/zenodo.17233543 (ref. 57). Source data are provided with this paper.

References

53. Deutsch, B., Hillenbrand, R. & Novotny, L. Near-field amplitude and phase recovery using phase-shifting interferometry. *Opt. Express* **16**, 494–501 (2008).
54. Woessner, A. et al. Highly confined low-loss plasmons in graphene–boron nitride heterostructures. *Nat. Mater.* **14**, 421–425 (2015).
55. Lorimor, O. G. & Spitzer, W. G. Infrared refractive index and absorption of InAs and CdTe. *J. Appl. Phys.* **36**, 1841–1844 (1965).
56. Esteban, R., Aizpurua, J. & Bryant, G. W. Strong coupling of single emitters interacting with phononic infrared antennae. *New J. Phys.* **16**, 013052 (2014).
57. Vicentini, E. Real-space observation of flat-band ultrastrong coupling between optical phonons and surface plasmon polaritons. *Zenodo* https://doi.org/10.5281/zenodo.17233543 (2025).

Acknowledgements

E.V. acknowledges funding from grant FJC2021-046779-I, financed by MICIU/AEI/10.13039/501100011033 and the European Union NextGenerationEU/PRTR, and from the European Union's Horizon Europe research and innovation programme under Marie Skłodowska-Curie grant agreement no. 101063152. The work also received financial support from grant CEX2020-001038-M, grant PID2021-123949GB-I00 (NANOSPEC) and grant PID2024-156602NB-I00 (CEDANO), funded by MICIU/AEI/10.13039/501100011033 and by ERDF/EU. J.A., R.E. and X.A. acknowledge funding from grant PID2022-139579NB-I00, funded by MICIU/AEI/10.13039/501100011033 and ERDF/EU; from project IT1526-22 from the Department of Science, Universities and Innovation of the Basque Government; and from Elkartek project 'u4smart' from the Department of Industry of the Basque Government. X.A. acknowledges the Spanish Ministerio de Ciencia, Innovación y Universidades for his grant, FPU21/02963. M.S. acknowledges financial support from grant PID2023-148359NB-C22 (AI-NANOSPEC), funded by MICIU/AEI/10.13039/501100011033 and ERDF/EU, and grant RYC2023-044188-I, funded by MICIU/AEI/10.13039/501100011033 and by FSE+.

Author contributions

E.V. and R.H. conceived the experiment. M.B.B. and M.R. prepared the samples. E.V., N.P. and F.B. performed the experiments. E.V. and X.A. developed and implemented the theoretical models and analysed the data. A.B. contributed to the dispersion calculations. M.S. performed numerical simulation. R.H. led the project. E.V., X.A., R.E., J.A. and R.H. co-wrote the paper with input from all co-authors. All authors contributed to discussions.

Competing interests

R.H. is a co-founder of Neaspec GmbH, which is now a part of Attocube Systems GmbH, a company producing s-SNOM systems such as the one used in this study. The other authors declare no competing interests.

Additional information

Supplementary information The online version contains supplementary material available at https://doi.org/10.1038/s41563-025-02412-6.

Correspondence and requests for materials should be addressed to Rainer Hillenbrand.

Peer review information *Nature Materials* thanks Wei Xiong and Joel Yuen-Zhou for their contribution to the peer review of this work.